Chemical Engineering Journal 446 (2022) 136966

Contents lists available at ScienceDirect

Chemical Engineering Journal

journal homepage: www.elsevier.com/locate/cej

Iterative redox activation promotes interfacial synergy in an Ag/Cu_xO catalyst for oxygen reduction

Youngtae Park [a,1], Kihyun Shin [b,1], Changsoo Lee [c,1], Sang-Yeon Lee [d], Yong-Kul Lee [d], Chang-Hee Kim [c,e], Hyun-Seok Cho [c,*], Graeme Henkelman [b,*], Hyuck Mo Lee [a,*]

[a] Department of Materials Science and Engineering, KAIST, 291 Daehak-ro, Yuseong-gu, Daejeon 34141, Republic of Korea
[b] Department of Chemistry, and the Oden Institute for Computational Engineering and Sciences, University of Texas at Austin, Austin, TX 78712, United States
[c] Hydrogen Research Department, Korea Institute of Energy Research (KIER), 152 Gajeong-ro, Yuseong-gu, Daejeon 34129, Republic of Korea
[d] Department of Chemical Engineering, Dankook University, 152 Jukjeon-ro, Yongin 16890, Republic of Korea
[e] School of Energy Technology, Korea Institute of Energy Technology, 200 Hyuksin-ro, Naju 58330, Republic of Korea

ARTICLE INFO

Keywords:
Electrocatalyst
Oxygen reduction
Iterative redox activation
Ag/metal oxide composite
Charge transfer

ABSTRACT

An iterative electrochemical activation process is demonstrated to maximize the interface between Ag and Cu_xO. Morphological reconstruction and phase transformation of Cu_xO occurs through the iterative electrochemical redox reaction, as indicated by energy-dispersive spectroscopy and X-ray photoelectron spectroscopy. The activated Ag/Cu_xO/C catalysts exhibits enhanced oxygen reduction reaction performance, with an onset potential of 0.86 V vs. the reversible hydrogen electrode, a Tafel slope of 46 mV dec^{-1}, and a high stability as compared to Ag/C. A mechanistic study using density functional theory shows that the weakened binding energy of the OH intermediate, originating from the charge transfer from Ag to Cu_xO, improves the ORR activity at the interface sites of the Ag/Cu_xO electrocatalysts. Ag/Cu_xO shows a higher limiting potential of 0.14 V for interface sites than isolated Ag nanoparticles. The interfacial charge transfer between Ag and CuO is verified experimentally.

1. Introduction

With growing concerns about global warming and climate change, renewable energy conversion and storage technologies have attracted attention for solving numerous challenging environmental issues [1–6]. Alkaline exchange membrane fuel cells (AEMFCs) have emerged as a promising technology for sustainable energy because of the wider range of material choices in alkaline media as compared to acidic media [7,8]. The cathodic reaction of AEMFCs, the oxygen reduction reaction (ORR), has sluggish kinetics as compared to the hydrogen oxidation reaction (HOR) [8], making this reduction reaction a rate-determining step for the overall reaction. Thus, developing non-Pt metal electrocatalysts with excellent activity and durability toward the ORR, comparable to Pt-based electrocatalysts, is of great importance.

Over the last decade, studies in theoretical computational materials science have led to the proposition of a volcano relation between the ORR catalytic activity and the adsorption energy of the key reaction intermediates, which clarifies the origin of the high catalytic activity of materials and suggests a strategy for catalytic activity improvement [9–12]. From this point of view, Ag is a promising material with excellent ORR activity in alkaline media due to its nearly optimal oxygen adsorption energy. In regard to its stability, the feasibility of using Ag in alkaline media has been validated from the surface Pourbaix diagram, which explains the pH-dependent stability of catalyst materials in ORR systems [13]. However, since Ag catalysts have relatively lower activity than commercial Pt/C, improving the catalytic activity for the ORR is required.

To promote the catalytic properties of Ag-based electrocatalysts, several approaches have been investigated, including morphology control [14–19], alloying with other elements [20–24], and combining with various metal oxides [25–29]. Among these studies, the electronic structure modification of Ag via interactions with a metal oxide is one of the most promising methods to improve its catalytic activity. Boskovic et al. investigated the electrochemical behavior of an Ag/TiO_2 composite for electrocatalysts [27]. Wang et al. showed the effect of Co_3O_4 as a support material for Ag catalyst [28]. Additionally, Kim et al.

* Corresponding authors.
E-mail addresses: hscho@kier.re.kr (H.-S. Cho), henkelman@utexas.edu (G. Henkelman), hmlee@kaist.ac.kr (H.M. Lee).
[1] Equal contributions.

https://doi.org/10.1016/j.cej.2022.136966
Received 1 March 2022; Received in revised form 9 May 2022; Accepted 10 May 2022
Available online 13 May 2022

reported the strong interactions between Ag and Mn_3O_4 of $Ag/Mn_3O_4/C$ electrocatalysts in alkaline media [26]. Although the strong interaction between Ag and metal oxides has been extensively studied, their positive effects are limited to the local interfaces between them. Thus, it is very important to maximize the interfacial area between Ag and metal oxides. However, studies based upon maximizing the interfacial area between Ag and metal oxides have rarely been reported.

A phase transformation of the metal oxide can increase the interfacial area between Ag and metal oxides. Copper oxide is a typical transition metal oxide, showing dramatic morphological changes upon phase transformation [30–32]. Cuprous oxide (Cu_2O, Cu^+) can be transformed to cupric oxide (CuO, Cu^{2+}) under thermal or electrochemical oxidizing conditions. During the phase transformation, the copper oxide undergoes a dramatic morphological change and volumetric expansion. For example, Al-Antaki et al. reported the morphology change of copper oxide during the phase transformation from cuprous oxide to cupric oxide [32]. Kim et al. found branched cupric oxide with a large active surface area from the controlled oxidation of cubic-type cuprous oxide [31]. Park et al. showed the conversion of cuprous oxide nanocubes to cupric oxide urchin-like nanostructures via a sequential dissolution-precipitation process during the oxidation reaction [30]. Such morphological reconstructions of copper oxide have been broadly applied in the development of electrocatalysts. Thus, one can expect that the phase transformation of copper oxide can be used to increase the interfacial area between silver and copper oxide, maximizing the metal–metal oxide interactions.

Herein, we developed a simple electrochemical activation method based on the iterative redox reaction deriving sequential dissolution/redeposition of Cu_xO in Ag/Cu_xO electrocatalysts. The phase transformation and the dramatic morphological changes of $Ag/CuO_x/C$ electrocatalysts were confirmed by scanning transmission electron microscopy (STEM), transmission electron microscopy (TEM), EDS, and X-ray diffraction (XRD). We also employed density functional theory (DFT) to identify the activity difference between the isolated Ag nanoparticles (NPs) and Ag NP/CuO_x support by calculating the reaction energy profile for the ORR. Based on the experimental results and DFT calculations, we discuss the strong interactions between the Ag NPs and the phase-transformed CuO_x layer, showing dramatically enhanced ORR activity and durability compared to Ag/C electrocatalysts.

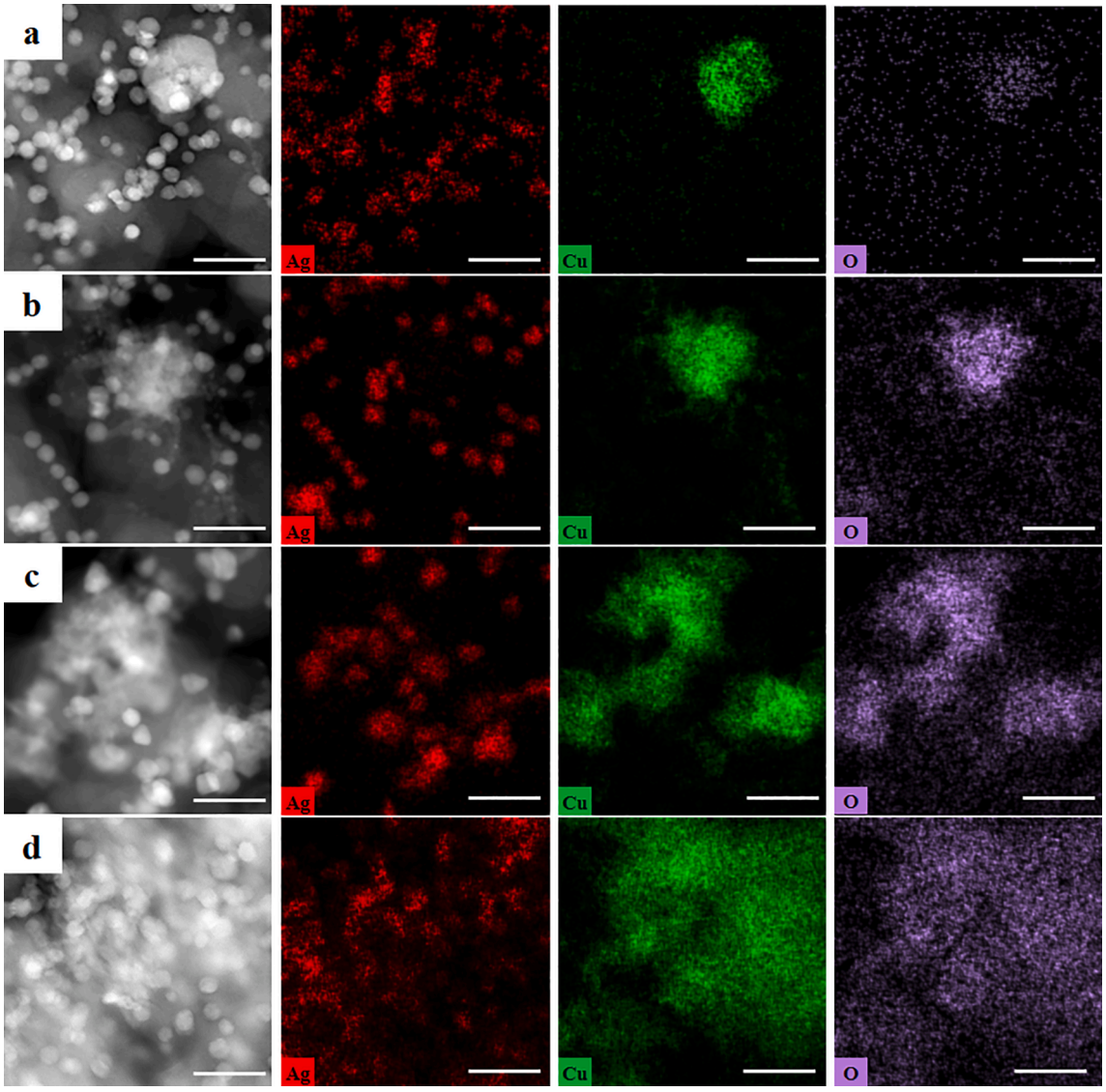

Fig. 1. HAADF-STEM and EDS elemental maps of $Ag/Cu_xO/C$ catalysts: (a) before activation and after activation for (b) 1 cycle, (c) 25 cycles, and (d) 50 cycles. Scale bars: (a)-(d) 40 nm.

2. Results and discussion

2.1. Morphological evolution via electrochemical activation

To investigate the interactions between Ag and Cu_xO, we synthesized Ag and Cu_2O NPs with a simple OAm-based wet-chemical method. The method used to synthesize monodispersed spherical Ag NPs was reported in our previous study [33,34]. Briefly, Ag NPs were synthesized using $AgNO_3$ precursors heated in OAm for 1 h at 180 °C and 5 h at 150 °C. The Cu_2O NPs were synthesized at 230 °C for 30 min using an OAm solution in which the $Cu(acac)_2$ precursor was dissolved at a high concentration [35]. Then, the synthesized Ag NPs, Cu_2O NPs, and carbon black were mixed by sonication and stirred in toluene for 1 day. We used a gravimetric ratio of 1:1:3 (Ag:Cu_2O:C) for the Ag/Cu_2O/C catalyst. To increase the interfacial area between Ag and Cu_xO in the Ag/Cu_xO/C electrocatalysts, an iterative electrochemical redox process was conducted by CV in the range of 0.515 – 0.915 V with a scan rate of 100 mV/s for 50 cycles. To confirm the morphological reconstruction of Cu_xO according to the number of electrochemical activation cycles, we conducted high-angle annular dark-field scanning transmission electron microscopy (HAADF-STEM) analysis (as shown in Fig. 1) of the Ag/Cu_xO/C catalyst: (a) before activation and after activation for (b) 1 cycle, (c) 25 cycles, and (d) 50 cycles. Before the activation of Ag/Cu_xO/C, Cu_2O showed a nanoplate morphology with clear boundaries, as shown in Fig. 1(a). Notably, the Ag NPs rarely come into contact with the Cu_2O NPs, and their interactions are limited to local interfaces. To increase the interfacial area between the Ag NPs and Cu_2O NPs, the amount of oxide is important. However, as the amount of Cu_2O NPs increases, the electronic conductivity of Ag/Cu_xO/C decreases [25]. Thus, to maximize the interaction points between the metal and metal oxide, we propose a facile electrochemical method that generates a high specific surface area of Cu_xO. During the phase transformation, there is a change in morphology and volumetric expansion of the copper oxide. For instance, copper oxide with a Cu_2O phase is transformed to a CuO phase with a higher volume and surface area upon electrochemical oxidation [31]. Thus, we used an electrochemical activation process, which iteratively converts Cu_2O to CuO by repeated redox reactions to increase the interfacial area between Ag and Cu_xO. After one activation cycle with an oxidation scan alone, a morphological reconstruction of copper oxide on Ag/Cu_xO/C was observed, as shown in Fig. 1(b). Based on the distribution of Cu and O, the copper oxide was slightly spread out. As shown in Fig. 1(c-d), as the number of activation cycles increased, the copper oxide spread more widely. Through 50 cycles of electrochemical activation, the copper oxide size increases by about 3.5 times compared to the initial nanoplate-shaped copper oxide. Compared with Ag/Cu_xO/C before activation, where Ag NPs and Cu_2O NPs rarely contact, Ag/Cu_xO/C activated by 50 cycles has dramatically increased interfaces between Ag and Cu_xO in Fig. 1(d). To confirm the elemental ratio of Ag and Cu, we measured the composition of Ag/Cu_xO/C before and after activation by EDS. The atomic compositions of Ag and Cu remained almost the same (before activation = 39.0:61.0, after activation = 39.1:60.9). This composition matched well with the designed Ag and Cu atomic ratio of Ag/Cu_xO/C (Ag:Cu = 40:60).

As shown in Fig. 2(a-b), the morphologies of Ag loaded on carbon with and without Cu_2O were observed with TEM analysis. The small dark-colored particles and the large dark-colored particles represent Ag NPs and Cu_2O NPs, respectively, whereas the light-colored particles are from the carbon support. The Ag NPs were uniformly dispersed on the supports and showed little agglomeration for both Ag/Cu_xO/C and Ag/C. As a result, Fig. 2(c) shows the widely spread, dark-colored Cu_xO nanosheets that were formed from Cu_2O NPs via the iterative electrochemical redox reactions. From the morphological reconstruction of Ag/Cu_xO/C after activation in Fig. 2(c), it should be noted that the contact points between Ag and Cu_xO were increased significantly compared to that of Ag/Cu_xO/C before activation. To clarify how electrochemical activation affects the morphology and size of the Ag NPs, we measured the size of the Ag NPs and plotted the particle size distribution on Ag/C and before and after activation Ag/Cu_xO/C, as shown in the insets of Fig. 2(a-c). It was confirmed that the activation process, in which the potential region affects the redox reaction of copper-based materials,

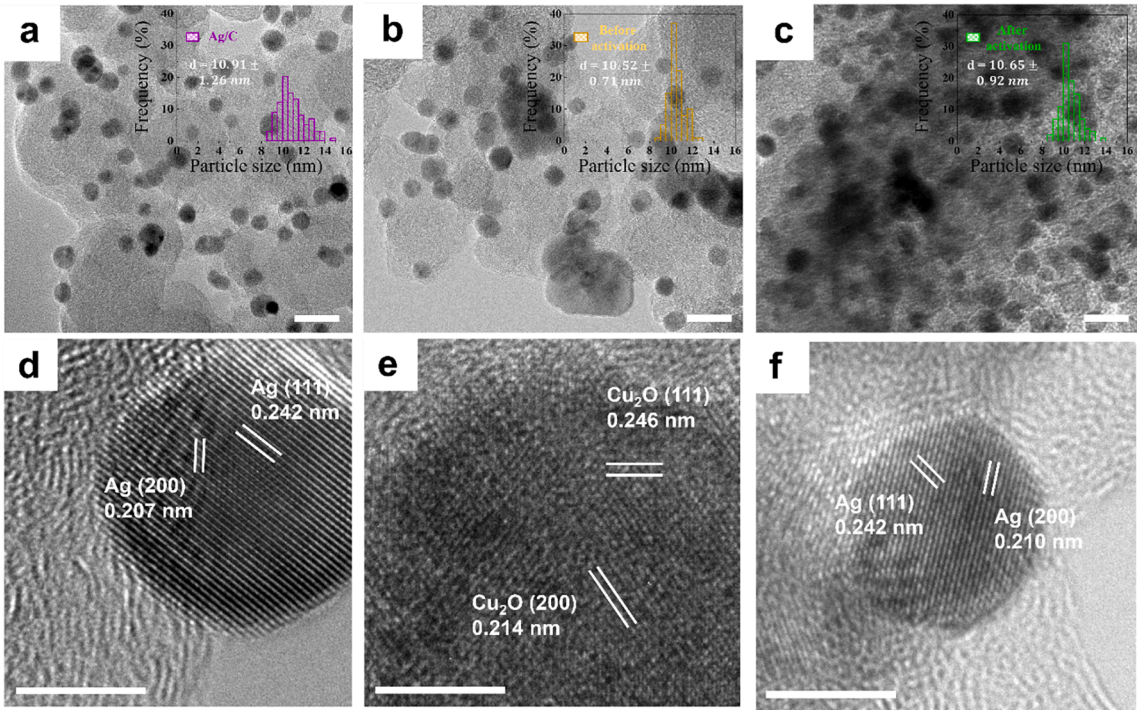

Fig. 2. TEM images of (a) Ag/C and Ag/Cu_xO/C: (b) before and (c) after activation. HRTEM images of (d) Ag and (e) Cu_2O on Ag/Cu_xO/C before activation, and (f) Ag on Ag/Cu_xO/C after activation. Insets are Ag nanoparticle size distributions on (a) Ag/C and Ag/Cu_xO/C: (b) before and (c) after activation, respectively. Scale bars: (a)-(c) 20 nm, (d)-(f) 5 nm.

does not transform the morphology and size of the Ag NPs. From the size distribution of Ag particles, we focused on the interactions between Ag and Cu_xO since both cases of Ag/Cu_xO/C have similar average particle size distributions of Ag NPs. High-resolution transmission microscopy (HRTEM) images of Cu_xO in Ag/Cu_xO/C before and after activation (see Fig. 2(d-f)) were obtained. As shown in the lattice fringes in Fig. 2(d) before activation, Ag/Cu_xO/C showed lattice spacings of 0.242 and 0.207 nm, which were assigned to the (111) and (200) planes of Ag, respectively [36,37]. After activation, the lattice spacing of Ag on Ag/Cu_xO/C (Fig. 2(f)) showed values (0.242 and 0.210 nm) similar to those before activation. The above results indicate that the Ag phase on Ag/Cu_xO/C did not change during the activation process. Furthermore, before the activation of Ag/Cu_xO/C, as shown in Fig. 2(e), lattice spacings of 0.246 and 0.214 nm were observed, corresponding to the (111) and (200) planes of cubic Cu_2O, respectively [38]. However, after activation, it was difficult to find any clear lattice fringes for copper oxide. The low crystallinity of the activated copper oxide likely resulted from the activation process spreading the copper oxide in the form of a thin film. Therefore, we successfully controlled the morphological reconstruction of Cu_xO and optimized the interfacial area between Ag and Cu_xO via electrochemical activation.

2.2. Phase transformation via electrochemical activation

To reveal the effect of electrochemical activation on the phase transformation, the crystal structures of the bulk phase Cu_xO on Ag/Cu_xO/C were investigated by XRD analysis, as shown in Fig. 3(a). For XRD analysis of the electrochemically activated sample, Ag/Cu_xO/C catalyst ink was dropped on the surface of a Ti foil to form a working electrode that was electrochemically activated. The diffraction peaks at 40.2° and 38.4° for both samples are indexed to the (101) and (002) crystal facets of hexagonal Ti (JCPDS No. 44-1294). The peaks at $2\theta =$ 38.3°, 44.5°, 64.7°, and 77.8° were assigned to the (111), (200), (220), and (311) crystal planes of face-centered cubic (FCC) Ag, respectively (JCPDS No. 87-0719) [39]. The crystal structure of Ag on Ag/Cu_xO/C was not changed during electrochemical activation, as shown in Fig. 3 (a). In the case of Ag/Cu_xO/C before activation, the crystal structure of Cu_2O matched that of cubic-phase Cu_2O (JCPDS No. 65-3288) [35,40,41], whereas the Cu_2O diffraction peaks vanished after activation. However, the first and second characteristic diffraction peaks of CuO (111) and ($\bar{1}$ 11) at 38.7° and 35.5° (monoclinic structure, JCPDS No. 80-1916) were not observed in Ag/Cu_xO/C after activation because the activated Cu_xO spread out to form an ultrathin layer with low crystallinity. Moreover, the primary diffraction peak of CuO overlapped with that of Ag (111). To confirm the phase transformation of copper oxide during electrochemical oxidation, activated Cu_xO/C loaded at 50 wt% Cu_2O on carbon black, which was higher than that of Ag/Cu_xO/C, was designed and characterized by XRD [42]. As shown in Fig. S1, the phase transformation from Cu_2O to CuO upon electrochemical activation was clearly visible.

XPS analysis of the Cu 2p core level was carried out to investigate the surface chemical state and compositional change of Cu_xO on Ag/Cu_xO/C

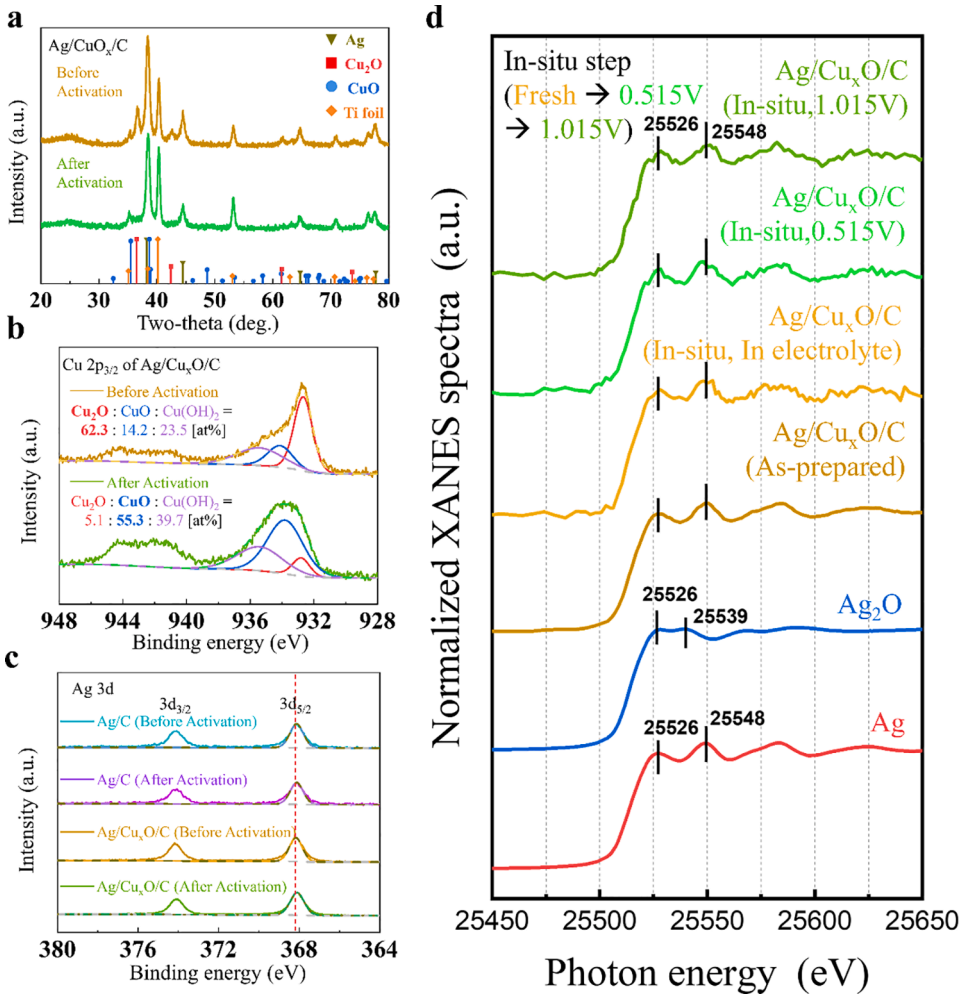

Fig. 3. Phase transformation upon activation; (a) XRD of Ag/Cu_xO/C, (b) XPS Cu $2p_{3/2}$ peaks of Ag/Cu_xO/C, (c) XPS Ag 3d peaks of Ag/C and Ag/Cu_xO/C, and (d) in situ XANES Ag K-edge of Ag/Cu_xO/C.

before and after activation. Fig. 3(b) shows the Cu $2p_{3/2}$ XPS spectra of Ag/Cu_xO/C before and after activation. The Cu $2p_{3/2}$ spectrum can be divided into three peaks, corresponding to CuO, Cu_2O, and $Cu(OH)_2$ at 932.6, 934, and 935.2 eV, respectively [43]. Quantitative analysis of the Cu_2O, CuO, and $Cu(OH)_2$ peaks revealed that before activation, the main phase of Cu_xO is Cu_2O. On the other hand, the peak of CuO increased noticeably after electrochemical activation. In addition, the intensity of the Cu $2p_{3/2}$ satellite peaks, which were observed in the CuO phase [44], increased upon activation. These results indicate that electrochemical oxidation can successfully transform the Cu_2O phase of Cu_xO into the CuO phase. Fig. 3(c) shows the XPS spectra of Ag 3d core levels. The binding energies of Ag $3d_{5/2}$ of Ag/C and Ag/Cu_xO/C before activation were 368.13 and 368.17 eV, respectively. After the activation process, the binding energy of Ag $3d_{5/2}$ on Ag/C (368.13 eV) remained nearly unchanged, while the binding energy of Ag $3d_{5/2}$ on Ag/Cu_xO/C (368.10 eV) was slightly shifted to lower energy. However, since all these binding energies are in a tolerance range of metallic silver (Ag^0, 368.2 eV), it is hard to clearly define the interaction between Ag and CuO [45].

To investigate the oxidation state change of Ag during the activation process, we conducted in situ X-ray absorption near edge structure (XANES) analysis. Fig. 3(d) shows the Ag K-edge in situ XANES spectra for Ag/Cu_xO/C catalysts. We also indicate the spectra of Ag and Ag_2O nanoparticles as reference. The XANES spectrum of as-prepared Ag/Cu_xO/C showed almost the same with Ag reference. For in situ XANES analysis, we firstly checked the open circuit voltage (OCV) state of Ag/Cu_xO/C in 0.1 M KOH. The XANES spectra showed no significant difference between the as-prepared and the electrolyte state Ag/Cu_xO/C. We proceed with an anodic scan of cyclic voltammetry (CV) to oxidize the Cu_2O to CuO. As a result, we couldn't find a discernible distinction between before oxidizing (0.515 V) and after oxidizing (1.015 V) of Cu_xO. This result is consistent with previous literature in which 8 nm Ag nanoparticles dispersed in CuO were confirmed to retain the metallic phase in XANES analysis [46]. Since XANES analysis focus on the core level change and bulk property, it is hard to distinguish the charge transfer that is occurred at the catalyst surface, especially at the local Ag/CuO interface.

The following is a summary of the findings from the XRD, XPS, and in situ XANES investigations. First, we observed the phase transition of Cu_xO before and after the activation. Cu_2O is the predominant phase of Cu_xO before activation, according to XRD and XPS studies. CuO, which forms as a result of the oxidation of Cu^{2+} species, is the most prevalent phase of Cu_xO in XPS results after activation. Second, we investigated the effect of Cu_xO phase on the chemical state of Ag. We were able to confirm that the chemical state of Ag is metallic silver (Ag^0) by XPS even when the predominat phase of Cu_xO is changed from Cu_2O to CuO. In situ XANES analysis showed that the chemical state of Ag was stable as Ag^0 in the ORR working environment. As a result we felt the necessity for a theoretical approach to understand the interaction between Ag and Cu_xO through the study of the phase and chemical state of Ag/Cu_xO/C catalysts.

2.3. Electrochemical behavior of Ag/Cu_xO/C

To investigate the redox behavior of our electrocatalysts, we carried out CV (10 mVs^{-1}) measurements of Ag/C and Ag/Cu_xO/C in N_2-saturated 0.1 M KOH, as shown in Fig. 4(a). During the oxidation of Ag on Ag/C, two anodic peaks were observed at 1.23 and 1.29 V, associated with the formation of AgOH and Ag_2O, respectively [47]. The cathodic peak of Ag hydroxide and oxides was located at 1.06 V. The morphology and peak potential in the CV curve are in good agreement with previously reported values. However, in the case of Ag/Cu_xO/C, the redox

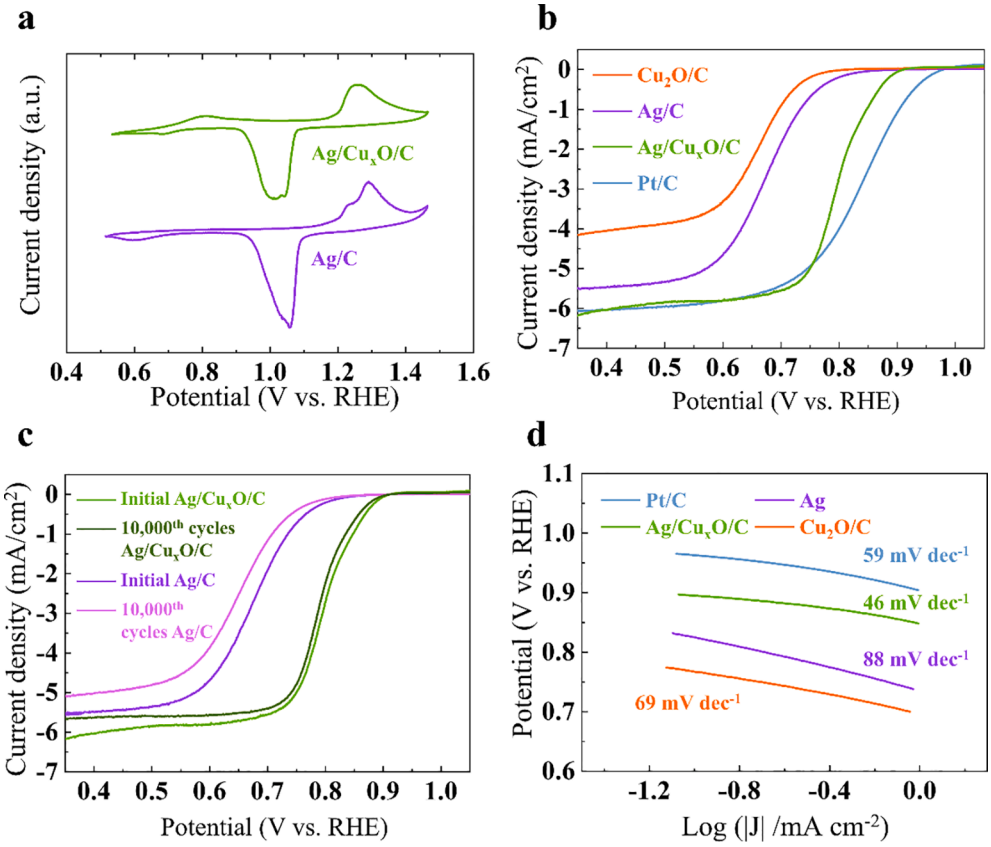

Fig. 4. Electrochemical measurements of Ag/C, Cu_xO/C, Pt/C and Ag/Cu_xO/C. (a) Cyclic voltammetry (CV) measurements in N_2-saturated 0.1 M KOH; (b) ORR polarization curves, (c) accelerated durability test (ADT), and (d) Tafel slopes; (b) - (d) measurements were conducted in O_2-saturated 0.1 M KOH.

peak potentials of Ag were shifted to more negative values compared with Ag/C, which means that the reducibility of Ag on Ag/Cu_xO/C is decreased [48]. Liu et al. reported that the negative shift of the CV peak potentials of Ag originated from electron donation from Ag [49]. Furthermore, as shown by the CV in Fig. S2, it is notable that the effect of Cu_xO redox on the CV of Ag/Cu_xO/C above 0.9 V is negligible. Therefore, the redox peak shift in the negative direction is evidence of charge transfer from Ag to Cu_xO. The oxidation and reduction couples of copper oxide were observed at 0.8 and 0.7 V, respectively. These peak potentials match well with the previously reported value.

To investigate the ORR activity, the polarization curves of Ag/C, Cu_xO/C, and Ag/Cu_xO/C were recorded at 1600 rpm in O_2-saturated 0.1 M KOH, as shown in Fig. 4(b). The half-wave potential of Ag/C was 0.67 V vs. reversible hydrogen electrode (RHE), which is in agreement with previously reported values [26,50]. In the case of Ag/Cu_xO/C before activation, the half-wave potential is higher than that of Ag/C, which corresponds to an enhancement in ORR activity (Fig. S3). However, the limited interface between Ag and Cu_xO cannot be entirely responsible for the performance of Ag/Cu_xO/C. Thus, electrochemical activation afforded a uniformly thin layer of Cu_xO on the carbon support, and the structure of this layer has been confirmed by other characterization methods. The optimized interfacial area between Ag and Cu_xO further increases the ORR activity of Ag/Cu_xO/C. The 100 mV shift in the onset potential from 0.76 V (Ag/C) to 0.86 V (Ag/Cu_xO/C) demonstrates that the interactions between Ag and the Cu_xO interface improved the catalytic activity of Ag. Moreover, there is a 130 mV shift of the half-wave potential ($E_{1/2}$) from the activated Ag/Cu_xO/C (0.80 V) to Ag/C (0.67 V). This trend is comparable to previous results for Ag-based alkaline ORR catalysts shown in Fig. S4, suggesting that activated Ag/Cu_xO/C is an efficient ORR catalyst. To clarify the origin of the catalytic activity improvement, the ORR activity of Cu_xO/C was examined. Cu_xO/C has a very low diffusion-limiting current and a poor half-wave potential compared to those of Ag/C and Ag/Cu_xO/C, indicating that the enhancement of the catalytic activity originates from the interactions between Ag and Cu_xO, not from Cu_xO itself. An addition of oxide material can possibly decrease an electrical conductivity of the electrocatalysts. Interestingly, Ag/Cu_xO/C showed a higher limiting current density than Ag/C. The enhanced interaction between Ag and Cu_xO is main reason for the higher limiting current density. Fig. 4(c) shows accelerated durability test (ADT) results to confirm the stability of Ag/Cu_xO/C. After 10,000 cycles, Ag/Cu_xO/C shows only a 10 mV decrease in the half-wave potential, which means it is more stable than Ag/C (23 mV). Moreover, as shown in Fig. 4(d), the smaller Tafel slope of Ag/Cu_xO/C (46 mV dec^{-1}) in the region of low overpotential indicates better ORR kinetics for Ag/Cu_xO/C than for Ag/C (88 mV dec^{-1}) in alkaline media. These results confirm that the activity and stability of the activated Ag/Cu_xO/C catalysts is superior to that of Ag/C for alkaline ORR.

2.4. Theoretical modeling of Ag NPs and Ag/CuO (001)

We found that the ORR activity and durability of Ag NPs can be increased with a CuO (001) support; however, the reason is yet unclear. Here, we aim to uncover the synergistic effects between Ag NP and the CuO (001) support by employing DFT calculations. When modeling both the isolated and supported Ag NPs, the cuboctahedral (COh) structure was used with careful consideration (see Fig. 5), even though COh is less stable than the icosahedron (Ih) structure by 0.03 eV/atom. There are several reasons for this: (1) Our main objective in this study is to understand the synergistic effects between the NPs and support, so we wanted to minimize differences such as the shape and size between the isolated and supported Ag NPs; (2) COh can be easily supported on the monoclinic CuO (001) surface because COh also has a (001) facet, which is well matched with CuO (001), and this is not possible in the Ih structure. Fundamentally, the COh structure is composed of seven (111) layers stacked in an ABC sequence because it is based on the FCC structure. To attach the Ag NPs to the CuO (001) surface, we cut the three bottom (111) layers off the NP, and placed them on the surface. As shown in Fig. 5(a-b), the Ag NPs are identical in terms of facets, shape, structure, and size regardless of the support, so we believe that these are ideal models to compare the differences between isolated and supported Ag NPs.

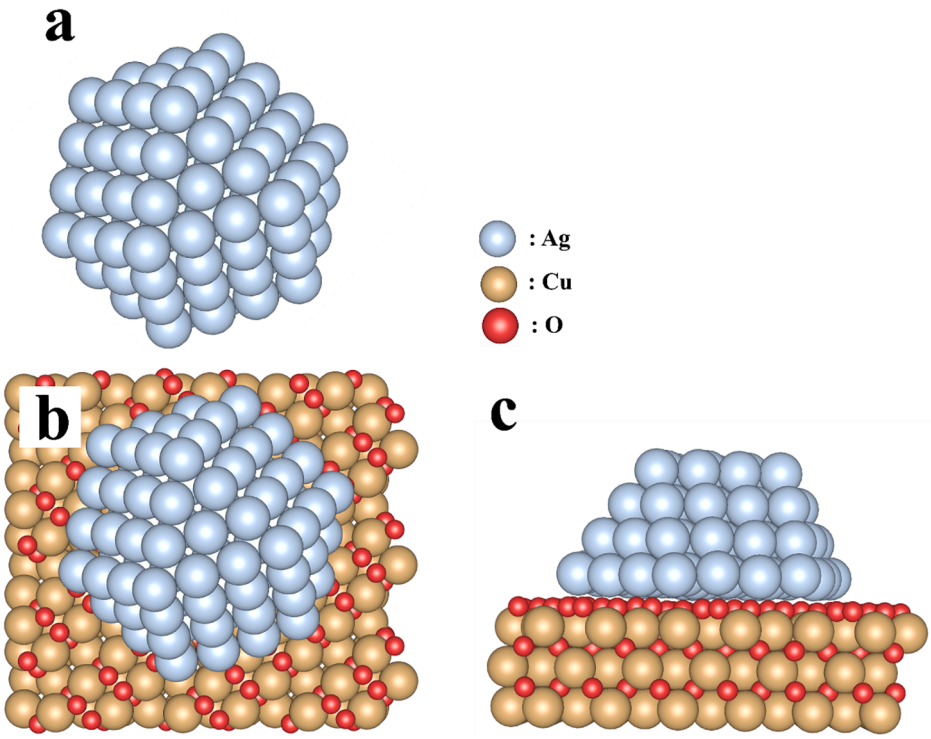

Fig. 5. Structure of Ag NP and Ag NP/CuO models: (a) Ag_{147} NP with COh structure; (b) top and (c) side view of the Ag_{92} NP supported on monoclinic CuO (001).

2.5. ORR activity of Ag NPs and Ag/CuO (001) by DFT calculations

To evaluate the ORR activity by DFT calculations, the binding energies of each intermediate (O*, OH*, and OOH*) were investigated using the Gibbs free energy diagram shown in Fig. S5. As expected, in the case of isolated Ag NPs, all of the intermediates were strongly adsorbed at the edge of the NP at sites with low coordination numbers (see Fig. S5 (a)); these binding energies are given in Table S1. According to our previous study, the ORR intermediates were stabilized at the edge of isolated Au NPs having the same COh structure as the Ag NPs in this study [51]. As shown in Fig. S5(a), the rate-determining step (RDS) on the Ag NPs is the last step (ΔG_4), which means that the strong OH* binding energy inhibits H_2O formation. Therefore, it is crucial to reduce the OH* binding energy to enhance the ORR activity.

For the Ag/CuO (001) calculations, two different types of reaction sites were considered: (1) the top of the supported Ag NP (Ag/CuO_top) and (2) the interface between the Ag NP and the CuO support (Ag/CuO_interface). The Gibbs free energy diagram and the binding energies of each intermediate for Ag/CuO are given in Fig. S5 and Table S1, respectively. Interestingly, both reaction sites for Ag/CuO showed higher limiting potentials (similar to the experimental onset potential) by 60 (Ag/CuO_top) and 140 mV (Ag/CuO_interface) than the isolated Ag NPs. The RDS was ΔG_4, which is the same as isolated Ag NPs, but the OH* binding energy is decreased. This was exactly what is needed to increase the ORR activity of isolated Ag NPs, as discussed in the previous paragraph. Thus, we focused on the OH* binding energies on isolated Ag and Ag/CuO by analyzing how and why the binding energies were decreased.

As mentioned in the previous section, Ag/CuO is structurally quite similar to isolated Ag NPs except for the Ag-Ag bond length and the charge state. Specifically, we found that supported Ag NPs were expanded to match the CuO lattice by an average of 17.23 Å (width) compared to isolated Ag NPs by 17.13 Å (width); as discussed in previous reports, tensile stress on the system typically increases the binding energy [50,52], and this was also seen in our system (the so-called strain effect) [51,53]. Supported Ag NPs were oxidized (-0.07 e/atom) by donating electrons to CuO. Furthermore, most electrons (-0.18 e/atom) are donated from the bottom layer, and the two topmost layers remain unchanged. These electron deficiencies are strongly related to the weak O* (OH* or OOH*) binding energy because of the high electronegativity of O. For OH* binding on Ag/CuO_top, the supported Ag NPs were expanded, but the charge state was unchanged; however, the OH* binding energy was decreased by 60 meV. This is due to the change in the stable binding site, as shown in Fig. S5(a-b). OH* was stabilized at the edge site of isolated Ag NPs, which is usually stable in most transition and noble metal systems; however, OH* on Ag/CuO_top was stabilized on the hollow site, and we already discussed OH* binding site changes in different systems when there is lattice expansion [54]. For OH* binding on the Ag/CuO_interface shown in Fig. S5(c), the Ag NPs were expanded but highly oxidized, so we expect the two opposite effects to cancel out; however, the OH* binding energy was 140 meV weaker than that of the isolated Ag NPs. This is because the OH* binding energy is not very sensitive to strain effects [52]; thus, the two effects do not cancel out; rather the highly oxidized charge state decreases the OH* binding energy. We found that the strain effect and charge transfer change the binding energies of intermediates especially OH*, which alter the ORR activity.

As we discussed in the last paragraph, the RDS for both isolated Ag NP and Ag/CuO catalyst was the last hydrogenation step (ΔG_4), which means the surface of catalysts could be poisoned by OH* species due to strong OH* binding. Thus, we made the surface Pourbaix energy diagram to find the stable OH*-coverage in the actual ORR working potential range (Fig. 6(a-b)). We sequentially increased the number of adsorbed OH* species until we obtained a clear diagram. In the case of the isolated Ag NP, 24OH* (0.15–0.30 V), 48OH* (0.30–0.67 V), and 60OH* (0.67 V~) coverages were the most stable in the specific

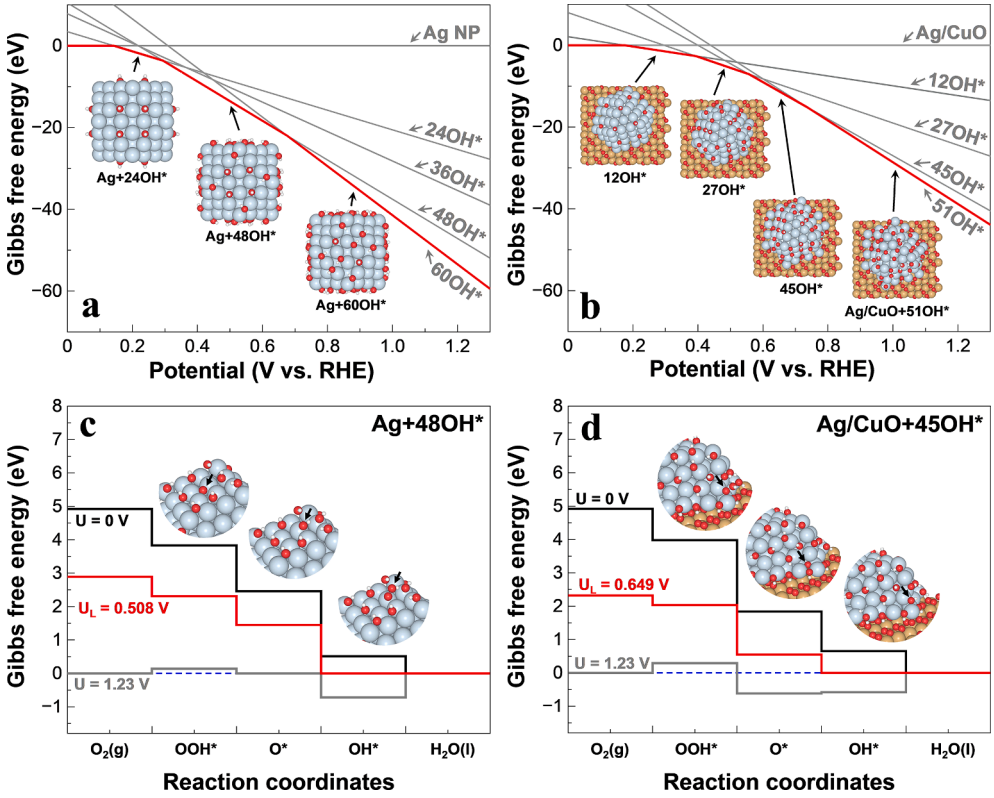

Fig. 6. Surface Pourbaix energy diagram for OH* coverage on the (a) isolated Ag NP and (b) Ag/CuO (001). Gibbs free energy diagram for ORR on (c) an OH*-covered isolated Ag NP and (d) interface site of Ag/CuO (001).

potential ranges. In the Ag/CuO catalyst system, 12OH* (0.18–0.40 V), 27OH* (0.40–0.56 V), 45OH* (0.56–0.75 V), and 51OH* (0.75 V~) coverages were also the most stable in the specific potential range. According to the experimental analysis in Fig. 4(b), ORR started at around 0.8 V for Ag/C (or 0.9 V for Ag/CuO), and the current density saturated at around 0.6 V (or 0.7 V), so the actual OH*-coverage could be 48 or 60OH* for Ag NP and 45 or 51OH* for Ag/CuO based on the stable potential range. Furthermore, we checked the OH* adsorption energy for each coverage and found that 48OH* for Ag and 45OH* for Ag/CuO is the most stable coverage; OH* adsorption energies including ΔZPE and TΔS for the Gibbs free energy calculation showed that 48OH* and 60OH* had 0.44 and 0.57 eV binding energies, respectively. Those values were in the range of stable 48OH* coverage by 0.30–0.67 V. In the same manner, OH* adsorption energies in 45OH* and 51OH* for Ag/CuO showed 0.58 and 0.68 eV, respectively, which are also in the 45OH* stable potential range of 0.56–0.75 V. Therefore, we used 48OH* coverage for isolated Ag NP and 45OH* coverage for Ag/CuO catalyst to calculate the ORR activity in actual working conditions.

We also separated two different reaction sites for Ag/CuO: top and interface site to see which reaction site is more active. We carefully tested all possible binding sites and calculated the binding energies at the most stable binding sites, as shown in Table S1. Finally, we made a reaction energy diagram for ORR on the OH* pre-covered Ag and Ag/CuO catalysts in Fig. 6(c-d). As we discussed before, we tested top and interface sites for 45OH* covered Ag/CuO. The interface sites showed a higher limiting potential (650 mV) than that of 48OH* covered Ag NP (510 mV), but the top site did not show any activity improvement (Fig. S6). From these results, we concluded that maximizing the interfaces between Ag and CuO could lead to high catalytic activity. We also found that the limiting potential differences (140 mV) were well matched with the experimental observation by 130 mV (half-wave potential).

2.6. Experimental verification of interfacial charge transfer

By employing DFT calculations, we could determine the synergetic effect between Ag and CuO that enhances the ORR catalytic activity. The charge transfer from Ag to CuO regulates the OH* binding energy, which is the most important intermediate determining the catalytic activity. However, in the XPS and in situ XANES spectra of Ag/Cu_xO/C, the charge transfer was ambiguous. As we confirmed in our DFT calculations, the limitation of experimental observation for charge transfer exists since the charge transfer occurs locally at the interface between Ag and CuO. Therefore, we designed a simple thin-film experiment to confirm the interfacial charge transfer between Ag and CuO.

For investigating the interfacial charge transfer, we prepared Ag/CuO thin film on Si wafer using physical vapor deposition (PVD) with different Ag deposition times (from 1s to 15 m). To exclude the interaction between CuO and Si, the CuO film is deposited thick enough for 4 hrs with 150 W of radio-frequency (RF) power and 5 mTorr of a pressure condition. We performed ex-situ XPS analysis on Ag/CuO thin film with different Ag deposition times Fig. 7(a)). As shown in Fig. 7(b), we observed a sequential redshift of the Ag 3d binding energy peaks as the deposition time decreased. This phenomenon supported the local charge transfer at the interface between Ag and CuO. As the deposition time increases to more than 1 min, the Ag $3d_{5/2}$ binding energy peak of Ag/CuO tends to be almost identical to that of metallic Ag (Ag^0, 368.2 eV). However, in short deposition times (1–3s), where the effect of the interaction between Ag and CuO is strong, the binding energy of Ag $3d_{5/2}$ is located near the Ag^+ binding energy (367.5 eV). As a result of the Ag/CuO thin film experiment, we validate the interfacial charge transfer between Ag and CuO.

3. Conclusion

In summary, using a simple electrochemical activation method, we developed a Ag/Cu_xO/C catalyst with an optimized interface between Ag and Cu_xO for significantly enhanced ORR catalytic activity compared to Ag/C. Moreover, we investigated the role of electronic effects between Ag and Cu_xO in the catalytic activity of Ag in the ORR under alkaline conditions. The activated Ag/Cu_xO/C exhibits a 130 mV of half-wave potential shift compared to Ag NPs and a 46 mV dec^{-1} Tafel plot slope for the alkaline ORR. To confirm the effects of electrochemical activation, we studied the morphological evolution and phase transformation of the Ag/Cu_xO/C catalyst. The iterative redox reaction on Ag/Cu_xO/C effectively spread out the copper oxide by dissolution and redeposition mechanisms. The HAADF-STEM, EDS maps, and HRTEM analysis clearly showed the morphological reconstruction in which the copper oxide gradually spread out as the number of electrochemical activation cycles increased. XRD and XPS analysis confirmed that the phase of copper oxide was successfully controlled by the sequential activation process. Furthermore, to understand the effects of Cu_xO on the electronic structure of Ag, we conducted both experimental and theoretical investigations. It is hard to determine the charge transfer between Ag and CuO through in situ XANES and XPS analysis, which represent bulk and surface properties, respectively. For exploring the synergy between Ag and CuO, we used DFT calculations to determine the atomic-scale interactions between Ag and CuO. Moreover, we could clarify the relation between charge transfer and the ORR activity enhancement. Especially due to the local charge transfer occurring at the interface between Ag and CuO, the weakened OH* binding energy of Ag/CuO resulted in improved catalytic activity, and the difference in the onset potential between the Ag NPs and Ag/CuO is in good agreement with the experimental value (100 mV). We demonstrate the interfacial charge transfer between Ag and CuO through the thin film experiment. As a result, using the electrochemical activation method, we have obtained a multifaceted understanding of the behavior and the electronic effects of Cu_xO, which provides new avenues for designing metal-

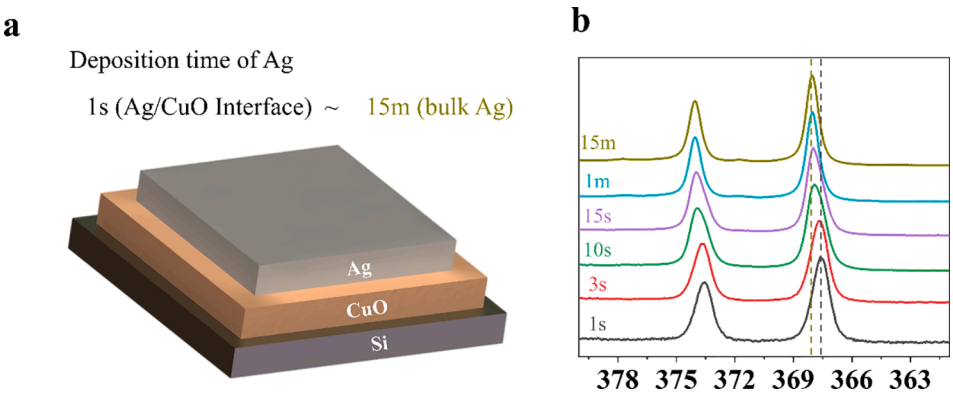

Fig. 7. (a) Scheme of Ag/CuO film on Si wafer (b) XPS Ag 3d peaks of Ag/CuO on Si wafer at different Ag deposition times.

reducible oxide systems with the increased interfacial area for ORR catalysts.

4. Experimental section

4.1. Materials

Copper(II) acetylacetonate ($Cu(acac)_2$, >99.9 %), silver nitrate ($AgNO_3$, >99.0 %), oleylamine (OAm, 70 %), toluene ($C_6H_5CH_3$, >99.5 %), potassium hydroxide (KOH, >99.99 %), and Nafion solution (5 wt% Nafion dissolved in alcohol) were purchased from Sigma Aldrich. Hexane (C_6H_{14}, 95 %) was purchased from Junsei Chemical Co., Ltd. A commercial Pt/C catalyst (nominally 20 wt% on carbon black) was purchased from Etek Company. Milli-Q ultrapure water (>18 MΩ·cm) was used in all experiments.

4.2. Synthesis of the Ag NPs

The Ag NPs were synthesized following the procedure reported in our previous work [33,34]. First, 2.5 g of $AgNO_3$ and 100 mL of OAm were added to a 250-mL three-neck flask under high purity Ar gas (99.99 %) with constant stirring. Then, for Ag nanoparticles with a narrow size distribution, we conducted a two-step synthesis involving a high-temperature (180 °C) ripening stage for 1 h and a low-temperature (150 °C) incubation stage for 5 h. Then, the reaction mixture was cooled and washed once with a mixture of ethanol and hexane. After washing, the Ag NPs were dried in a vacuum oven at 45 °C for 4 h.

4.3. Synthesis of the Cu_2O NPs

Cu_2O was synthesized via a simple wet-chemical method. First, 15 g of $Cu(acac)_2$ and 100 mL of OAm were added to a 250-mL three-neck flask under ambient conditions with constant stirring. To synthesize the Cu_2O NPs, we heated the solution at 230 °C for 30 min. Then, the reaction mixture was cooled and washed once with a mixture of ethanol and hexane. After washing, the Cu_2O NPs were dried in a vacuum oven at 45 °C for 4 h.

4.4. Preparation of the carbon-supported catalysts

To explore the interactions between Ag and CuO_x, we prepared three types of catalysts: Ag/C, Cu_xO/C, and Ag/Cu_xO/C. To load nanoparticles onto carbon, carbon black (Vulcan XC 72R) was dispersed in toluene by ultrasonication for 1 h. Ag and Cu_2O NPs were also dispersed in toluene and then added to the above dispersion containing carbon black. The gravimetric ratios of Ag/C, Cu_xO/C, and Ag/Cu_xO/C were set to 1:4, 1:4, and 1:1:3, respectively. After that, the final mixture was ultrasonicated for 1 h and stirred for 1 d. The mixtures were centrifuged at 8,000 rpm for 20 min and washed three times with a mixture of hexane and ethanol. The catalysts were dried in a vacuum oven at 45 °C for 12 h.

4.5. Material characterization

The morphologies of the catalysts were observed by TEM (Technai G2 F30 S-Twin, FEI). High-angle annular dark-field scanning transmission electron microscopy (HAADF-STEM) and EDS measurements were carried out on a 200 kV Talos F200X instrument. The crystal structures of the catalysts were characterized using high-resolution X-ray diffractometry (HRXRD) (SmartLab, RIGAKU). The X-ray radiation was Cu K α operated at 45 kV and 200 mA. The chemical state of the elements was verified using XPS (K-Alpha+, Thermo Fisher Scientific) with Al Kα radiation (1486.6 eV). The binding energy data was calibrated using carbon 1s as a reference (binding energy of C 1s = 284.8 eV). The X-ray absorption near-edge structure spectroscopy (XANES) measurements were conducted at Ag K-edge (25,514 eV) on the beamlines of the Pohang Light Source (PLS) (8C and 10C), which has a flux of 5×10^{12} photons s^{-1} at 300 mA and 2.5 GeV. A customized cell was used in the fluorescence mode for in situ XANES measurements. The ink-deposited carbon paper (1.5 × 1.5 cm^2) was used as a working electrode in the in situ cell, which was filled with 0.1 M KOH, as seen in Fig. S7. The counter and reference electrodes were a Pt coil and a Hg/HgO electrode, respectively. Ex situ XANES spectra for Ag and Ag_2O reference samples were also obtained. The Winxas 3.1 program was used to remove the background and normalize the XANES spectra.

4.6. Electrochemical measurements

The electrochemical measurements of the electrocatalysts were carried out using a conventional three-electrode cell and a potentiostat (interface 1010E, Gamry). A graphite rod and Hg/HgO (filled with 20 wt % KOH) were used as the counter and reference electrodes, respectively. The potentials measured in this work were converted to a reversible hydrogen electrode (RHE) scale by standard calibration in an H_2-purged 0.1 M KOH solution prior to measurement. All the electrochemical measurements were iR-corrected using the CI method implemented in Gamry software. Ten milligrams of the catalyst were dispersed in a mixture of 1.0 mL of IPA, 1.0 mL of DI water, and 50 μ L of 5 % Nafion® 117 solution under ultrasonication for 30 min. The catalyst ink (10 μ L) was dropped onto a glassy carbon electrode with a diameter of 5 mm (geometrical area = 0.196 cm^2, Pine Instruments) and dried under an IR lamp for 15 min. All catalysts were activated by repeated cyclic voltammetry (CV) in the range of 0.515 – 0.915 V with a scan rate of 100 mV/s for 50 cycles before electrochemical measurements. CV curves were obtained by cycling the potential between 0.515 and 1.465 V in an N_2-saturated 0.1 M KOH solution at a scan rate of 50 mV/s. The ORR polarization curves were measured by sweeping the potential between 0.334 and 1.084 V in an O_2-saturated 0.1 M KOH solution with a scan rate of 10 mV/s and a rotating speed of 1600 rpm. The accelerated durability test (ADT) was performed by CV between 0.415 and 1.015 V for 10,000 cycles in an O_2-saturated 0.1 M KOH solution with a scan rate of 500 mV/s.

4.7. Computational details

GGA-level, spin-polarized DFT calculations were performed with the Vienna ab-initio simulation package using a plane-wave basis set with a cut-off energy of 400 eV. The Perdew-Burke-Ernzerhof functional was used to describe electron exchange and correlation [55,56]. The DFT + U method was employed to treat localized Cu 3d orbitals with an effective U value of 7.0 eV, as reported in a previous paper [57]. The Brillouin zone was sampled at the gamma point in both the NP and NP/support calculations, which was found to be sufficient given the large system size. The convergence criteria for the electronic and geometric optimizations were 10^{-5} eV and 10^{-2} eV/Å, respectively.

The monoclinic CuO (0 0 1) structure was modeled based on experimental observations of the phase transformation from Cu_2O to CuO (which will be discussed later in the results section) and previous reports that the CuO (0 0 1) facet has the highest activity among the low-index facets [50,58]. The cuboctahedral structure (COh) of Ag NPs with 147 atoms was modeled and isolated with a 10 Å vacuum gap in all directions to avoid self-interaction. All atoms were fully relaxed in the calculations. The same COh structure was also used to model Ag NPs supported on a CuO (0 0 1) slab (Ag/CuO (0 0 1)), which had a 20 Å vacuum gap in the z-direction; the bottom CuO layer was fixed in the bulk positions. To calculate the ORR activity, the following four associative reaction steps were considered.

$$\Delta G_1 : O_2(g) + H^+ + e^- + * \leftrightarrow OOH^* \quad (1)$$

$$\Delta G_2 : OOH^* + H^+ + e^- \leftrightarrow O^* + H_2O(l) \quad (2)$$

$$\Delta G_3 : O^* + H^+ + e^- \leftrightarrow OH^* \quad (3)$$

$$\Delta G_4 : OH^* + H^+ + e^- \leftrightarrow H_2O(l) + * \quad (4)$$

The ORR overpotential (η) was found from the reaction energy diagram drawn with the following equations (Eq. (5) and Eq. (6)) [10].

$$\Delta G(U) = \Delta E + \Delta ZPE - T\Delta S + neU \quad (5)$$

$$\eta = 1.23 - U_L \quad (6)$$

where ΔE is the reaction energy, ΔZPE is the zero-point energy correction, ΔS is the change in entropy, U is the applied potential, and U_L is the limiting potential. The chemical potential of the solvated proton and electron pair ($H^+ + e^-$) under standard conditions ($p_{H_2} = 1$ bar, $a_{H^+} = 1$, T = 298.15 K) was calculated as 0.5 $\mu^0_{H_2(g)}$ $-eU$ by assuming equilibrium at the standard hydrogen electrode [59,60]. Solvation effects, modeled by surrounding the adsorbed species with water molecules, were included in the calculated reaction energy diagrams [61].

Declaration of Competing Interest

The authors declare that they have no known competing financial interests or personal relationships that could have appeared to influence the work reported in this paper.

Acknowledgements

This work was supported by the National Research Foundation of Korea (NRF) grant funded by the Korean government (MSIT) (No. 2017R1E1A1A03071049, 2020R1A5A6017701, and 2019M3E6A1064020). The computation work at UT Austin was supported by the Department of Energy (DE-SC0010576) and the Welch Foundation (F-1841). Computational resources were provided by the Texas Advanced Computing Center and the National Energy Research Scientific Computing Center.

Appendix A. Supplementary data

Supplementary data to this article can be found online at https://doi.org/10.1016/j.cej.2022.136966.

References

[1] K. Zeng, X. Zheng, C. Li, J. Yan, J.H. Tian, C. Jin, P. Strasser, R. Yang, Recent advances in non-noble bifunctional oxygen electrocatalysts toward large-scale production, Adv. Funct. Mater. (2020) 1–23, https://doi.org/10.1002/adfm.202000503, 2000503.
[2] C. Lee, K. Shin, C. Jung, P.P. Choi, G. Henkelman, H.M. Lee, Atomically embedded ag via electrodiffusion boosts oxygen evolution of coooh nanosheet arrays, ACS Catal. 10 (2020) 562–569, https://doi.org/10.1021/acscatal.9b02249.
[3] W. Zhong, B. Xiao, Z. Lin, Z. Wang, L. Huang, S. Shen, Q. Zhang, L. Gu, RhSe 2: a superior 3D electrocatalyst with multiple active facets for hydrogen evolution reaction in both acid and alkaline solutions, Adv. Mater. 33 (2021) 2007894, https://doi.org/10.1002/adma.202007894.
[4] J.-Y. Zhang, Y. Yan, B. Mei, R. Qi, T. He, Z. Wang, W. Fang, S. Zaman, Y. Su, S. Ding, B.Y. Xia, Local spin-state tuning of cobalt–iron selenide nanoframes for the boosted oxygen evolution, Energy Environ. Sci. 14 (2021) 365–373, https://doi.org/10.1039/D0EE03500A.
[5] Y. Wang, X. Li, M. Zhang, J. Zhang, Z. Chen, X. Zheng, Z. Tian, N. Zhao, X. Han, K. Zaghib, Y. Wang, Y. Deng, W. Hu, Highly active and durable single-atom tungsten-doped NiS 0.5 Se 0.5 nanosheet@NiS 0.5 Se 0.5 nanorod heterostructures for water splitting, Adv. Mater. (2022) 2107053, https://doi.org/10.1002/adma.202107053.
[6] X. Han, X. Wu, Y. Deng, J. Liu, J. Lu, C. Zhong, W. Hu, Ultrafine Pt nanoparticle-decorated pyrite-type CoS 2 nanosheet arrays coated on carbon cloth as a bifunctional electrode for overall water splitting, Adv. Energy Mater. 8 (2018) 1800935, https://doi.org/10.1002/aenm.201800935.
[7] X. Ge, A. Sumboja, D. Wuu, T. An, B. Li, F.W.T. Goh, T.S.A. Hor, Y. Zong, Z. Liu, Oxygen reduction in alkaline media: from mechanisms to recent advances of catalysts, ACS Catal. 5 (2015) 4643–4667, https://doi.org/10.1021/acscatal.5b00524.
[8] H.A. Firouzjaie, W.E. Mustain, Catalytic advantages, challenges, and priorities in alkaline membrane fuel cells, ACS Catal. 10 (2020) 225–234, https://doi.org/10.1021/acscatal.9b03892.
[9] A. Kulkarni, S. Siahrostami, A. Patel, J.K. Nørskov, Understanding catalytic activity trends in the oxygen reduction reaction, Chem. Rev. 118 (2018) 2302–2312, https://doi.org/10.1021/acs.chemrev.7b00488.
[10] J.K. Nørskov, J. Rossmeisl, A. Logadottir, L. Lindqvist, J.R. Kitchin, T. Bligaard, H. Jónsson, Origin of the overpotential for oxygen reduction at a fuel-cell cathode, J. Phys. Chem. B. 108 (2004) 17886–17892, https://doi.org/10.1021/jp047349j.
[11] J. Greeley, I.E.L. Stephens, A.S. Bondarenko, T.P. Johansson, H.A. Hansen, T. F. Jaramillo, J. Rossmeisl, I. Chorkendorff, J.K. Nørskov, Alloys of platinum and early transition metals as oxygen reduction electrocatalysts, Nat. Chem. 1 (2009) 552–556, https://doi.org/10.1038/nchem.367.
[12] J. Greeley, J.K. Nørskov, Combinatorial density functional theory-based screening of surface alloys for the oxygen reduction reaction, J. Phys. Chem. C. 113 (2009) 4932–4939, https://doi.org/10.1021/jp808945y.
[13] H.A. Hansen, J. Rossmeisl, J.K. Nørskov, Surface Pourbaix diagrams and oxygen reduction activity of Pt, Ag and Ni(111) surfaces studied by DFT, Phys. Chem. Chem. Phys. 10 (2008) 3722–3730, https://doi.org/10.1039/b803956a.
[14] N. Wang, X. Cao, Q. Chen, G. Lin, Ag nanobelts: synthesis, morphological evolution, and their use as electrocatalysts for oxygen reduction, Chem. – A Eur. J. 18 (2012) 6049–6054, https://doi.org/10.1002/chem.201103926.
[15] Y. Lu, Y. Wang, W. Chen, Silver nanorods for oxygen reduction: Strong effects of protecting ligand on the electrocatalytic activity, J. Power Sources. 196 (2011) 3033–3038, https://doi.org/10.1016/j.jpowsour.2010.11.119.
[16] J. Ohyama, Y. Okata, N. Watabe, M. Katagiri, A. Nakamura, H. Arikawa, K. I. Shimizu, T. Takeguchi, W. Ueda, A. Satsuma, Oxygen reduction reaction over silver particles with various morphologies and surface chemical states, J. Power Sources. 245 (2014) 998–1004, https://doi.org/10.1016/j.jpowsour.2013.07.034.
[17] J.Y. Park, W.J. Dong, S.-M. Jung, Y.-T. Kim, J.-L. Lee, Oxygen reduction reaction of vertically-aligned nanoporous Ag nanowires, Appl. Catal. B Environ. 298 (2021), 120586, https://doi.org/10.1016/j.apcatb.2021.120586.
[18] M. Scherzer, F. Girgsdies, E. Stotz, M.-G. Willinger, E. Frei, R. Schlögl, U. Pietsch, T. Lunkenbein, Electrochemical surface oxidation of copper studied by in situ grazing incidence X-ray diffraction, J. Phys. Chem. C. 123 (2019) 13253–13262, https://doi.org/10.1021/acs.jpcc.9b00282.
[19] Z. Wang, X. Cao, D. Peng, Y. Lu, B. Zhang, K. Huang, T. Zhang, J. Wu, Y. Huang, Strained ultralong silver nanowires for enhanced electrocatalytic oxygen reduction reaction in alkaline medium, J. Phys. Chem. Lett. 12 (2021) 2029–2035, https://doi.org/10.1021/acs.jpclett.1c00249.
[20] X. Wu, F. Chen, N. Zhang, A. Qaseem, R.L. Johnston, Engineering bimetallic Ag–Cu nanoalloys for highly efficient oxygen reduction catalysts: a guideline for designing Ag-based electrocatalysts with activity comparable to Pt/C-20%, Small 13 (2017) 1–13, https://doi.org/10.1002/smll.201603876.
[21] A. Holewinski, J.-C. Idrobo, S. Linic, High-performance Ag–Co alloy catalysts for electrochemical oxygen reduction, Nat. Chem. 6 (2014) 828–834, https://doi.org/10.1038/nchem.2032.
[22] C.F. Calver, P. Dash, R.W.J. Scott, Selective hydrogenations with Ag, Pd catalysts prepared by galvanic exchange reactions, ChemCatChem. 3 (2011) 695–697, https://doi.org/10.1002/cctc.201000346.
[23] R.C. Sekol, X. Li, P. Cohen, G. Doubek, M. Carmo, A.D. Taylor, Silver palladium core–shell electrocatalyst supported on MWNTs for ORR in alkaline media, Appl. Catal. B Environ. 138–139 (2013) 285–293, https://doi.org/10.1016/j.apcatb.2013.02.054.
[24] S. Choi, Y. Park, J. Choi, C. Lee, H.S. Cho, C.H. Kim, J. Koo, H.M. Lee, Structural effectiveness of AgCl-decorated Ag nanowires enhancing oxygen reduction, ACS Sustain. Chem. Eng. 9 (2021) 7519–7528, https://doi.org/10.1021/acssuschemeng.1c01156.
[25] W. Wang, J.Q. Chen, Y.R. Tao, S.N. Zhu, Y.X. Zhang, X.C. Wu, Flowerlike Ag-supported Ce-doped Mn3O4 nanosheet heterostructure for a highly efficient oxygen reduction reaction: roles of metal oxides in Ag surface states, ACS Catal. 9 (2019) 3498–3510, https://doi.org/10.1021/acscatal.8b04943.
[26] S.A. Park, H. Lim, Y.T. Kim, Enhanced oxygen reduction reaction activity due to electronic effects between Ag and Mn3O4 in alkaline media, ACS Catal. 5 (2015) 3995–4002, https://doi.org/10.1021/acscatal.5b00495.
[27] I. Boskovic, S.V. Mentus, M. Pjescic, Electrochemical behavior of an Ag/TiO 2 composite surfaces, Electrochim. Acta. 51 (2006) 2793–2799, https://doi.org/10.1016/j.electacta.2005.07.054.
[28] Y. Wang, X. Lu, Y. Liu, Y. Deng, Silver supported on Co3O4 modified carbon as electrocatalyst for oxygen reduction reaction in alkaline media, Electrochem. Commun. 31 (2013) 108–111, https://doi.org/10.1016/j.elecom.2013.03.017.
[29] S. Liu, X. Qin, Preparation of a Ag–MnO 2 /graphene composite for the oxygen reduction reaction in alkaline solution, RSC Adv. 5 (2015) 15627–15633, https://doi.org/10.1039/C5RA00280J.
[30] J.C. Park, J. Kim, H. Kwon, H. Song, Gram-scale synthesis of Cu2O nanocubes and subsequent oxidation to CuO hollow nanostructures for lithium-ion battery anode materials, Adv. Mater. 21 (2009) 803–807, https://doi.org/10.1002/adma.200800596.
[31] J. Kim, W. Choi, J.W. Park, C. Kim, M. Kim, H. Song, Branched copper oxide nanoparticles induce highly selective ethylene production by electrochemical carbon dioxide reduction, J. Am. Chem. Soc. 141 (2019) 6986–6994, https://doi.org/10.1021/jacs.9b00911.
[32] A.H.M. Al-Antaki, X. Luo, X. Duan, R.N. Lamb, W.D. Hutchison, W. Lawrance, C. L. Raston, Continuous flow copper laser ablation synthesis of copper(I and II) oxide nanoparticles in water, ACS Omega 4 (2019) 13577–13584, https://doi.org/10.1021/acsomega.9b01983.
[33] I. Jung, K. Shin, N.R. Kim, H.M. Lee, Synthesis of low-temperature-processable and highly conductive Ag ink by a simple ligand modification: the role of adsorption

energy, J. Mater. Chem. C. 1 (2013) 1855–1862, https://doi.org/10.1039/c2tc00450j.
[34] I. Jung, Y.H. Jo, I. Kim, H.M. Lee, A simple process for synthesis of Ag nanoparticles and sintering of conductive ink for use in printed electronics, J. Electron. Mater. 41 (2012) 115–121, https://doi.org/10.1007/s11664-011-1761-3.
[35] C. Lee, K. Shin, Y.J. Lee, C. Jung, H.M. Lee, Effects of shell thickness on Ag-Cu2O core-shell nanoparticles with bumpy structures for enhancing photocatalytic activity and stability, Catal. Today. 303 (2018) 313–319, https://doi.org/10.1016/j.cattod.2017.08.016.
[36] E. Rodríguez-León, R. Iñiguez-Palomares, R. Navarro, R. Herrera-Urbina, J. Tánori, C. Iñiguez-Palomares, A. Maldonado, Synthesis of silver nanoparticles using reducing agents obtained from natural sources (Rumex hymenosepalus extracts), Nanoscale Res. Lett. 8 (2013) 318, https://doi.org/10.1186/1556-276X-8-318.
[37] M.R. Guascito, E. Filippo, C. Malitesta, D. Manno, A. Serra, A. Turco, A new amperometric nanostructured sensor for the analytical determination of hydrogen peroxide, Biosens. Bioelectron. 24 (2008) 1057–1063, https://doi.org/10.1016/j.bios.2008.07.048.
[38] D. Zhao, C.M. Tu, X.J. Hu, N. Zhang, Notable in situ surface transformation of Cu2O nanomaterials leads to dramatic activity enhancement for CO oxidation, RSC Adv. 7 (2017) 37596–37603, https://doi.org/10.1039/c7ra05950g.
[39] S.A. Chala, M.C. Tsai, W.N. Su, K.B. Ibrahim, B. Thirumalraj, T.S. Chan, J.F. Lee, H. Dai, B.J. Hwang, Hierarchical 3D architectured Ag nanowires shelled with NiMn-layered double hydroxide as an efficient bifunctional oxygen electrocatalyst, ACS Nano 14 (2020) 1770–1782, https://doi.org/10.1021/acsnano.9b07487.
[40] C.S. Choi, Y.U. Park, H. Kim, N.R. Kim, K. Kang, H.M. Lee, Three-dimensional sponge-like architectured cupric oxides as high-power and long-life anode material for lithium rechargeable batteries, Electrochim. Acta. 70 (2012) 98–104, https://doi.org/10.1016/j.electacta.2012.03.037.
[41] M. Balık, V. Bulut, I.Y. Erdogan, Optical, structural and phase transition properties of Cu2O, CuO and Cu2O/CuO: their photoelectrochemical sensor applications, Int. J. Hydrogen Energy. 44 (2019) 18744–18755, https://doi.org/10.1016/j.ijhydene.2018.08.159.
[42] N.R. Kim, I. Jung, Y.H. Jo, H.M. Lee, A simple process for the preparation of copper (I) oxide nanoparticles by a thermal decomposition process with borane tert-butylamine complex, J. Nanosci. Nanotechnol. 13 (2013) 6027–6032, https://doi.org/10.1166/jnn.2013.7649.
[43] S.D. Giri, A. Sarkar, Electrochemical study of bulk and monolayer copper in alkaline solution, J. Electrochem. Soc. 163 (2016) H252–H259. https://doi.org/10.1149/2.0071605jes.
[44] T. Balkan, H. Küçükkeçeci, H. Zarenezhad, S. Kaya, Ö. Metin, One-pot synthesis of monodisperse copper–silver alloy nanoparticles and their composition-dependent electrocatalytic activity for oxygen reduction reaction, J. Alloys Compd. 831 (2020) 154787.
[45] S.W. Gaarenstroom, N. Winograd, Initial and final state effects in the ESCA spectra of cadmium and silver oxides, J. Chem. Phys. 67 (1977) 3500–3506, https://doi.org/10.1063/1.435347.
[46] N. Ghasemi, F. Jamali-Sheini, R. Zekavati, CuO and Ag/CuO nanoparticles: biosynthesis and antibacterial properties, Mater. Lett. 196 (2017) 78–82, https://doi.org/10.1016/j.matlet.2017.02.111.
[47] J. Guo, A. Hsu, D. Chu, R. Chen, Improving oxygen reduction reaction activities on carbon-supported Ag nanoparticles in alkaline solutions, J. Phys. Chem. C. 114 (2010) 4324–4330, https://doi.org/10.1021/jp910790u.
[48] D.A. Slanac, W.G. Hardin, K.P. Johnston, K.J. Stevenson, Atomic ensemble and electronic effects in Ag-rich AgPd nanoalloy catalysts for oxygen reduction in alkaline media, J. Am. Chem. Soc. 134 (2012) 9812–9819, https://doi.org/10.1021/ja303580b.
[49] J. Liu, J. Liu, W. Song, F. Wang, Y. Song, The role of electronic interaction in the use of Ag and Mn3O4 hybrid nanocrystals covalently coupled with carbon as advanced oxygen reduction electrocatalysts, J. Mater. Chem. A. 2 (2014) 17477–17488, https://doi.org/10.1039/c4ta03937h.
[50] D. Higgins, M. Wette, B.M. Gibbons, S. Siahrostami, C. Hahn, M. Escudero-Escribano, M. García-Melchor, Z. Ulissi, R.C. Davis, A. Mehta, B.M. Clemens, J. K. Nørskov, T.F. Jaramillo, Copper silver thin films with metastable miscibility for oxygen reduction electrocatalysis in alkaline electrolytes, ACS Appl. Energy Mater. 1 (2018) 1990–1999, https://doi.org/10.1021/acsaem.8b00090.
[51] A. Galyamova, K. Shin, G. Henkelman, R.M. Crooks, Effect of TiO x substrate interactions on the electrocatalytic oxygen reduction reaction at Au nanoparticles, J. Phys. Chem. C. 124 (2020) 10045–10056, https://doi.org/10.1021/acs.jpcc.0c02754.
[52] S. Sharma, C. Zeng, A.A. Peterson, Face-centered tetragonal (FCT) Fe and Co alloys of Pt as catalysts for the oxygen reduction reaction (ORR): a DFT study, J. Chem. Phys. 150 (4) (2019) 041704.
[53] H. Li, K. Shin, G. Henkelman, Effects of ensembles, ligand, and strain on adsorbate binding to alloy surfaces, J. Chem. Phys. 149 (17) (2018) 174705.
[54] J.T.L. Gamler, K. Shin, H.M. Ashberry, Y. Chen, S.L.A. Bueno, Y. Tang, G. Henkelman, S.E. Skrabalak, Intermetallic Pd3Pb nanocubes with high selectivity for the 4-electron oxygen reduction reaction pathway, Nanoscale 12 (2020) 2532–2541, https://doi.org/10.1039/c9nr09759g.
[55] J.P. Perdew, K. Burke, M. Ernzerhof, Generalized gradient approximation made simple, Phys. Rev. Lett. 77 (1996) 3865–3868, https://doi.org/10.1103/PhysRevLett.77.3865.
[56] Y. Zhang, W. Yang, Comment on "Generalized Gradient Approximation Made Simple," Phys. Rev. Lett. 80 (1998) 890–890. https://doi.org/10.1103/PhysRevLett.80.890.
[57] K. Bhola, J.J. Varghese, L. Dapeng, Y. Liu, S.H. Mushrif, Influence of Hubbard U parameter in simulating adsorption and reactivity on CuO: combined theoretical and experimental study, J. Phys. Chem. C. 121 (2017) 21343–21353, https://doi.org/10.1021/acs.jpcc.7b05385.
[58] D. Su, X. Xie, S. Dou, G. Wang, CuO single crystal with exposed 001 facets-A highly efficient material for gas sensing and Li-ion battery applications, Sci. Rep. 4 (2014) 1–9, https://doi.org/10.1038/srep05753.
[59] I.C. Man, H.Y. Su, F. Calle-Vallejo, H.A. Hansen, J.I. Martínez, N.G. Inoglu, J. Kitchin, T.F. Jaramillo, J.K. Nørskov, J. Rossmeisl, Universality in oxygen evolution electrocatalysis on oxide surfaces, ChemCatChem 3 (2011) 1159–1165, https://doi.org/10.1002/cctc.201000397.
[60] A.A. Peterson, F. Abild-Pedersen, F. Studt, J. Rossmeisl, J.K. Nørskov, How copper catalyzes the electroreduction of carbon dioxide into hydrocarbon fuels, Energy Environ. Sci. 3 (2010) 1311–1315, https://doi.org/10.1039/c0ee00071j.
[61] S. Liu, M.G. White, P. Liu, Mechanism of oxygen reduction reaction on Pt(111) in alkaline solution: importance of chemisorbed water on surface, J. Phys. Chem. C 120 (2016) 15288–15298, https://doi.org/10.1021/acs.jpcc.6b05126.